Communicationless Reactance Compensation Using PWM-Controlled Switched Capacitors for Wireless Power Transfer

Ryo Matsumoto, *Graduate Student Member, IEEE*, Toshiyuki Fujita, *Member, IEEE*, and Hiroshi Fujimoto, *Senior Member, IEEE*

***Abstract*—Self-inductance variations caused by component tolerance and aging decrease the efficiency of wireless power transfer (WPT) systems. This article deals with this issue by compensating for the self-inductance variations using pulsewidth-modulation-controlled switched capacitors. Previous methods relied on wireless communication between the transmitter (Tx) and receiver (Rx) to control the variable capacitors, which is not a feasible approach when considering practical constraints. This article proposes a control scheme in which the switched capacitors are controlled simultaneously by separate closed loops on the Tx and Rx sides, thus eliminating wireless communication. The control scheme is based on a unique condition for perfect resonance derived by focusing on the output power of the WPT circuit. This article also points out the necessity to compensate for the self-inductance variations of both the Tx and Rx coils to achieve maximum ac/ac efficiency in battery charging applications. Furthermore, the proposed control scheme incorporates the soft-switching condition of the inverter to improve the dc/dc efficiency. Experimental results of a 1-kW prototype show that the switched capacitors can flexibly adapt to the self-inductance variations and improve the ac/ac efficiency and dc/dc efficiency by up to 3.04% and 8.63%, respectively.**

***Index Terms*—Component tolerance, resonant frequency, self-tuning, switched capacitor, wireless power transfer (WPT).**

I. Introduction

WIRELESS power transfer (WPT) is considered as a safe and convenient way to provide power to a wide range of applications, such as consumer electronics [1] and electric vehicles [2]. Among several types of WPT technologies, the magnetic resonance coupling can achieve high efficiency and high power over large air gaps, thus maximizing the benefits of WPT [3]. These attractive features are typically achieved by canceling the reactance of the transmitter (Tx) and receiver (Rx) coils with compensation capacitors [4], [5].

However, in practical WPT applications, the following factors cause the parameters of the coils and capacitors to vary from their designed values, thus preventing the reactance from being completely compensated. The first factor is the manufacturing tolerance and aging of the coils and capacitors. The manufacturing errors of mass-produced electronic components are inevitable. The second factor is the variation in the relative position of the Tx and Rx coils. The ferrite block and aluminum shield equipping the Tx coil affect the self-inductance of the Rx coil and vice-versa. This causes the self-inductance of the Tx and Rx coils to vary depending on their relative position [6], [7]. The third factor is the existence of other magnetic and conductive materials in the surrounding environment [8], [9]. For instance, if the Tx and Rx pads are installed near structures containing ferrous materials, the self-inductance of the coils will be affected.

By actively compensating the unnecessary reactance, the system can maintain the ideal performance even when the parameters of circuit components vary from their designed values. In the literature, several methods have been proposed to accomplish this goal using variable capacitors [10], [11], [12], [13], [14], [15], [16], [17], [18] and active rectifiers [19], [20], [21], [22].

In [10], [11], and [12], the resonance condition is maintained by switching the series and parallel connection of multiple capacitors. However, this method requires numerous switches and capacitors that increase the volume and cost of the system.

Several subsequent studies [13], [14], [15], [16], [17], [18] have adopted variable capacitor circuits in which the equivalent capacitance is controlled by the gate signals of the MOSFETs. In [14], a pulsewidth modulation (PWM) controlled switched capacitor is adopted on the Tx side to compensate for the self-inductance variation of the Tx coil. In [15], the self-inductance variation of the Rx coil is compensated by a PWM-controlled switched capacitor on the Rx side. However, Kim et al. [14], [15] do not consider the scenario where the self-inductance of the Tx and Rx coils varies simultaneously. The authors in [16], [17], and [18] adopt switch-controlled capacitors (SCCs) to compensate for the self-inductance variations of both the Tx and Rx coils. However, in [16], the control scheme for the Rx-side SCC has not been investigated. In [17], the SCCs are controlled based

Manuscript received 17 November 2022; revised 6 February 2023, 1 April 2023, and 13 June 2023; accepted 29 June 2023. Date of publication 12 July 2023; date of current version 1 September 2023. This work was supported in part by JST MIRAI under Grant JPMJMI21E2, in part by JSPS KAKENHI under Grant JP18H03768, in part by JST CREST under Grant JPMJCR15K3, and in part by CMK CORPORATION. Recommended for publication by Associate Editor D. Qiu. *(Corresponding author: Ryo Matsumoto.)*

The authors are with the Department of Advanced Energy, Graduate School of Frontier Sciences, The University of Tokyo, Chiba 277-8561, Japan (e-mail: 6077032961@edu.k.u-tokyo.ac.jp; t-fujita@edu.k.u-tokyo.ac.jp; fujimoto@k.u-tokyo.ac.jp).

Color versions of one or more figures in this article are available at https://doi.org/10.1109/TPEL.2023.3294487.

Digital Object Identifier 10.1109/TPEL.2023.3294487

on the parameter recognition, which is a complicated procedure and requires several circuit parameters to be premeasured. The control scheme in [18] requires wireless communication to obtain the amplitude of the Tx current on the Rx side. However, wireless communication increases the complexity of the system and entails the risk of communication failures, packet losses, and delays.

Other studies have adopted methods to control the phase-shift angle of the active rectifier [19], [20], [21]. However, these methods can only compensate for the unnecessary reactance in the Rx circuit. In order to compensate for the unnecessary reactance in both the Tx and Rx circuits, an additional degree of freedom is required.

In [22], the frequency of the inverter and the phase-shift angle of the semibridgeless active rectifier are controlled to compensate for the self-inductance variations of the Tx and Rx coils. In [23] and [24], variable capacitors are adopted to maintain the resonance condition in multireceiver WPT systems. The phase difference between the Tx and Rx currents plays an important role in the control schemes in [22], [23], and [24]. Wireless communication is required to compare the instantaneous phase of the Tx and Rx currents. However, this is not a practical solution when considering the latency of wireless communication, as discussed in Section II-A.

In practical WPT applications, the coils and capacitors of both the Tx and Rx sides are subject to parameter variations. However, none of the previous studies have proposed methods to simultaneously compensate for the unnecessary reactance in the Tx and Rx circuits without wireless communication.

This article proposes a control scheme for PWM-controlled switched capacitors to compensate for the self-inductance variations of the Tx and Rx coils without wireless communication. The control scheme is based on a unique condition for perfect resonance derived through the steady-state analysis of the WPT circuit. The information of the voltage and current phase of the Tx circuit is used to control the Tx-side switched capacitor. On the other hand, the information of the output power is used to control the Rx-side switched capacitor. The control scheme has the following advantages.

1) The self-inductance variations of the Tx and Rx coils can be simultaneously compensated.
2) Wireless communication is not required since the switched capacitors are controlled by separate closed loops on the Tx and Rx sides.

The basic idea of the control scheme was presented in our recent conference paper [25]. However, the control scheme was derived under several specific assumptions in order to simplify the analysis. Therefore, the generality of the proposed control scheme is clarified in this article through a comprehensive analysis of the WPT circuit. Moreover, in [25], the optimal condition in terms of the end-to-end system efficiency was not investigated. This article proposes an updated version of the control scheme in which the inverter efficiency is improved without sacrificing the ac/ac efficiency. This article also includes experimental results obtained under diverse patterns of self-inductance variations in order to demonstrate the versatility of the control scheme.

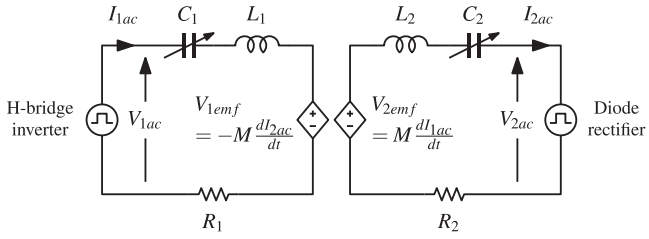

Fig. 1. Simplified model of an S–S compensated WPT circuit adopting variable capacitors.

The rest of this article is organized as follows. Section II discusses the conditions for perfect resonance and derives a unique condition, which is the underlying principle of the proposed control scheme. Section III describes the proposed control scheme in detail and explains how it can be further modified to improve the end-to-end system efficiency. Section IV presents the experimental results of a 1-kW prototype. Finally, Section V concludes this article.

II. Conditions for Perfect Resonance

This section focuses on the problem of how to determine whether or not the self-inductance variations are perfectly compensated by the variable capacitors. This problem is referred to as the condition for perfect resonance and formulates the underlying principle of the proposed control scheme. In Section II-A, conventional conditions for perfect resonance and their major drawbacks are described. In Section II-B, a unique condition for perfect resonance is derived to overcome the drawbacks of the conventional methods.

A. Conventional Conditions for Perfect Resonance

Fig. 1 shows a simplified model of an S–S compensated WPT circuit. Variable capacitors are adopted instead of passive capacitors to compensate for the self-inductance variations of the Tx and Rx coils. L, C, and R with subscripts 1 and 2 represent the coil's self-inductance, the variable capacitance, and the equivalent series resistance (ESR) of the Tx and Rx sides. M represents the mutual inductance between the Tx and Rx coils. $V_{1\mathrm{ac}}$ and $V_{2\mathrm{ac}}$ represent the terminal voltages of the inverter and rectifier. $I_{1\mathrm{ac}}$ and $I_{2\mathrm{ac}}$ represent the Tx and Rx currents. $V_{1\mathrm{emf}}$ and $V_{2\mathrm{emf}}$ represent the electromotive force induced in the Tx and Rx coils.

It is well known that high efficiency and high power are achieved under the perfect resonance condition

$$\omega = \frac{1}{\sqrt{L_1 C_1}} = \frac{1}{\sqrt{L_2 C_2}} \tag{1}$$

where ω is the operating angular frequency of the inverter [4]. When L_1 and L_2 vary from their designed values, the optimal condition can be maintained by controlling C_1 and C_2 to satisfy (1). However, this requires the values of L_1 and L_2 to be measured beforehand using external equipment. Since this is not a practical solution, an alternative information to evaluate the resonance condition is necessary.

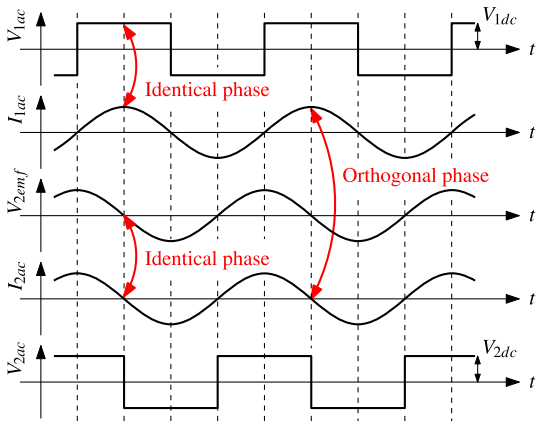

Fig. 2. Waveforms of V_{1ac}, I_{1ac}, V_{2emf}, I_{2ac}, and V_{2ac} under the perfect resonance condition.

The most basic approach is to use the information of the voltage phase and the current phase. Fig. 2 shows the waveforms of V_{1ac}, I_{1ac}, V_{2emf}, I_{2ac}, and V_{2ac} under the perfect resonance condition in (1). It is well known that under the optimal condition, the phase of V_{1ac} and I_{1ac} becomes identical, and the phase of V_{2emf} and I_{2ac} becomes identical as well [21]. Therefore, the condition for perfect resonance can be redescribed as follows:

$$\angle \dot{V}_{1ac} = \angle \dot{I}_{1ac} \wedge \angle \dot{V}_{2emf} = \angle \dot{I}_{2ac}. \tag{2}$$

In other words, the perfect resonance condition can be achieved by controlling C_1 and C_2 to satisfy (2). However, this is not a practical solution either since V_{2emf} cannot be measured directly.

It is also well known that when the circuit is in perfect resonance, the phase of V_{1ac} and I_{1ac} becomes identical, and the phase of I_{2ac} leads I_{1ac} by 90° [22], [23], [24]. Therefore, the condition for perfect resonance can be redescribed as follows:

$$\angle \dot{V}_{1ac} = \angle \dot{I}_{1ac} \wedge \angle \dot{I}_{2ac} = \angle \dot{I}_{1ac} + \frac{\pi}{2}. \tag{3}$$

V_{1ac}, I_{1ac}, and I_{2ac} are measurable. However, wireless communication between the Tx and Rx sides is required to obtain the phase difference between I_{1ac} and I_{2ac}. Wireless communication increases the complexity of the system and entails the risk of communication failures. Moreover, it is impractical to compare the instantaneous phase of I_{1ac} and I_{2ac} when considering the latency of wireless communication. For instance, the typical operating frequency for wireless EV charging is 85 kHz. On the other hand, the latency of wireless communication is in the order of milliseconds [26], which is several orders of magnitude longer than the period of an 85 kHz sine wave. In order to control the variable capacitors, a condition for perfect resonance, which can be evaluated without wireless communication, is necessary.

B. Proposed Condition for Perfect Resonance

Another unique condition for perfect resonance can be derived by focusing on the output power of the WPT circuit. The condition for perfect resonance can be redescribed as follows:

$$\angle \dot{V}_{1ac} = \angle \dot{I}_{1ac} \wedge P_2 = \min\left\{ P_2 \,\middle|\, \angle \dot{V}_{1ac} = \angle \dot{I}_{1ac} \right\} \tag{4}$$

where P_2 represents the output power of the WPT circuit. In fact, the perfect resonance condition is achieved when the output power is minimized under $\angle \dot{V}_{1ac} = \angle \dot{I}_{1ac}$. This condition is equivalent to the conditions in (1)–(3). The derivation of (4) is explained in the rest of this section.

Under the fundamental harmonic approximation, the input power and the output power are given by

$$P_1 = R_1|\dot{I}_{1ac}|^2 + R_2|\dot{I}_{2ac}|^2 + |\dot{V}_{2ac}||\dot{I}_{2ac}| \tag{5}$$

$$P_2 = |\dot{V}_{2ac}||\dot{I}_{2ac}|. \tag{6}$$

The reactance of the Tx circuit and the reactance of the Rx circuit are defined as follows:

$$X_1 := \omega L_1 - \frac{1}{\omega C_1}, \quad X_2 := \omega L_2 - \frac{1}{\omega C_2}. \tag{7}$$

X_1 and X_2 are equal to zero under the perfect resonance condition. Based on this definition, p_1 and p_2 are defined as per-unit expressions of P_1 and P_2 as follows:

$$p_1 := \frac{P_1(X_1, X_2)}{P_1(X_1=0, X_2=0)}, \quad p_2 := \frac{P_2(X_1, X_2)}{P_2(X_1=0, X_2=0)}. \tag{8}$$

p_1 and p_2 quantify how much the input power and the output power fluctuate from their optimal values according to X_1 and X_2. In addition, q_1, q_2, x_1, and x_2 are defined as nondimensional expressions of R_1, R_2, X_1, and X_2 as follows:

$$q_1 := \frac{\omega\sqrt{L_1L_2}}{R_1}, \quad q_2 := \frac{\omega\sqrt{L_1L_2}}{R_2} \tag{9}$$

$$x_1 := \frac{X_1}{\omega\sqrt{L_1L_2}}, \quad x_2 := \frac{X_2}{\omega\sqrt{L_1L_2}}. \tag{10}$$

q_1 and q_2 represent the quality factors of the Tx and Rx coils. x_1 and x_2 represent the percentage of self-inductance variations. R_1, R_2, X_1, and X_2 are normalized by $\omega\sqrt{L_1L_2}$ to express p_1 and p_2 in terms of completely nondimensional parameters. In this way, p_1 and p_2 can be calculated without specifying the values of L_1, L_2, R_1, R_2, and so on, thus performing the analysis in a generalized manner.

The coupling coefficient between the Tx and Rx coils is defined as $k := \frac{M}{\sqrt{L_1L_2}}$.

From Fig. 2, the root-mean-square values of V_{1ac} and V_{2ac} can be expressed in terms of V_{1dc} and V_{2dc} as follows:

$$|\dot{V}_{1ac}| = \frac{2\sqrt{2}}{\pi}V_{1dc}, \quad |\dot{V}_{2ac}| = \frac{2\sqrt{2}}{\pi}V_{2dc}. \tag{11}$$

In practical WPT applications, the inverter and rectifier are usually interfaced to constant voltage (CV) dc buses. In wireless EV charging, the rectifier is directly connected to the battery, or a dc/dc converter is connected between the rectifier and the battery [27]. Assuming that the output voltage of the battery is constant, V_{1dc} and V_{2dc} can be treated as constants when analyzing the circuit characteristics [28], [29]. Therefore, λ is defined as the ratio of V_{1dc} and V_{2dc} as follows:

$$\lambda := \frac{V_{1dc}}{V_{2dc}}. \tag{12}$$

By solving Kirchhoff's voltage law (KVL) equations derived from Fig. 1 with respect to (5)–(12), p_1 and p_2 can be expressed

in terms of nondimensional parameters as follows:

$$p_1 = \frac{\left(\frac{1}{q_1 q_2} + k^2\right)\left[\frac{x_2^2}{q_1} + \left(\frac{1}{q_2} + \zeta\right)\left(\frac{\zeta}{q_1} + \frac{1}{q_1 q_2} + k^2\right)\right]}{\zeta^2 k^2 \left(\lambda k + \frac{\lambda^2}{q_2}\right)} \tag{13}$$

$$p_2 = \frac{\frac{1}{q_1 q_2} + k^2}{\zeta\left(\lambda k - \frac{1}{q_1}\right)} \tag{14}$$

where

$$\zeta := \frac{\beta + \sqrt{\beta^2 + \alpha\gamma}}{\alpha} \tag{15}$$

$$\alpha := \lambda^2 k^2 - \frac{1}{q_1^2} - x_1^2 \tag{16}$$

$$\beta := \frac{1}{q_1}\left(\frac{1}{q_1 q_2} + k^2\right) + \frac{x_1 x_2}{q_2} \tag{17}$$

$$\gamma := \left(\frac{1}{q_1 q_2} + k^2 - x_1 x_2\right)^2 + \left(\frac{x_1}{q_2} + \frac{x_2}{q_1}\right)^2. \tag{18}$$

In addition, the phase difference between $\dot{V}_{1\mathrm{ac}}$ and $\dot{I}_{1\mathrm{ac}}$ can be derived as follows:

$$\theta := \angle\dot{V}_{1\mathrm{ac}} - \angle\dot{I}_{1\mathrm{ac}} = \arctan\left(\frac{x_1\left(\zeta^2 + x_2^2\right) - x_2 k^2}{\zeta k^2}\right). \tag{19}$$

The detailed derivation of (13)–(19) is given in Appendix A.

Fig. 3 shows the colormaps of p_1 and p_2 as functions of x_1 and x_2 under three cases of k and λ. The colormaps are obtained under $q_1 = q_2 = 400$. The contour lines of $\theta = -10°$, $\theta = 0$, and $\theta = 10°$ are also plotted on the colormaps of p_2. In all cases, the perfect resonance point, i.e., $x_1 = x_2 = 0$ coincides with the minimum point of p_2 on the contour line of $\theta = 0$. In other words, the perfect resonance condition is achieved when the output power is minimized under $\theta = 0$.

The same conclusion can be drawn from a numerical approach. When R_1 and R_2 are sufficiently small, the following approximation can be made:

$$\frac{1}{q_1} \approx 0, \quad \frac{1}{q_2} \approx 0. \tag{20}$$

By substituting (20) and $\theta = 0$ into (19), the following relationship between x_1 and x_2 can be derived:

$$x_2 = \frac{1}{\lambda^2} x_1. \tag{21}$$

By substituting (20) and (21) into (14), p_2 can be expressed as a convex downward function under $\theta = 0$ as follows:

$$p_2 = \frac{\lambda k}{\sqrt{\lambda^2 k^2 - x_1^2}} = \frac{k}{\sqrt{k^2 - \lambda^2 x_2^2}}. \tag{22}$$

Equation (22) indicates that the minimum point of p_2 under $\theta = 0$ is given by $x_1 = x_2 = 0$. In other words, the perfect resonance condition is achieved when the output power is minimized under $\theta = 0$. Therefore, the condition for perfect resonance can be expressed as in (4). It should be noted that the proposed condition for perfect resonance is valid for any given coupling coefficient and dc bus voltage ratio.

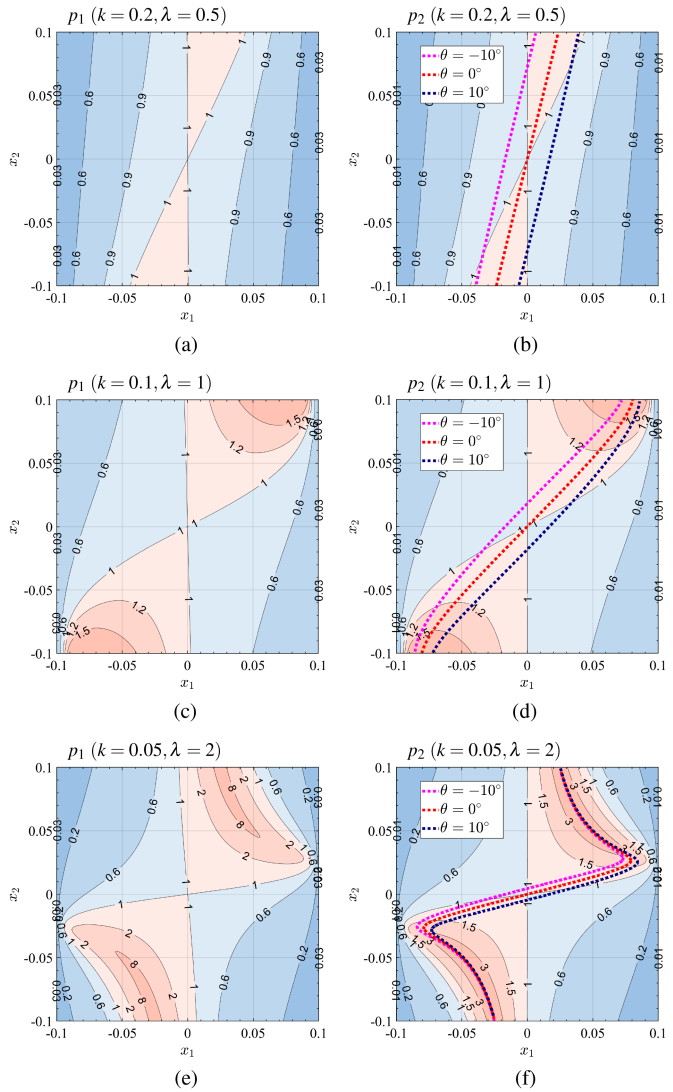

Fig. 3. Colormaps of p_1 and p_2 as functions of x_1 and x_2 under $q_1 = q_2 = 400$. (a) p_1 under $k = 0.2$ and $\lambda = 0.5$. (b) p_2 under $k = 0.2$ and $\lambda = 0.5$. (c) p_1 under $k = 0.1$ and $\lambda = 1$. (d) p_2 under $k = 0.1$ and $\lambda = 1$. (e) p_1 under $k = 0.05$ and $\lambda = 2$. (f) p_2 under $k = 0.05$ and $\lambda = 2$.

Based on (4), the variable capacitors can be controlled to maintain the perfect resonance condition without wireless communication.

III. Proposed Control Scheme

A. Outline of the Proposed Control Scheme

Based on (4), the perfect resonance condition described in (1)–(4) can be achieved by controlling the variable capacitors, as shown in Fig. 4. This control scheme simultaneously performs the following two functions.

1) The phase difference between $V_{1\mathrm{ac}}$ and $I_{1\mathrm{ac}}$ is controlled to $\theta_r = 0$ by adjusting the Tx-side variable capacitor.
2) The output power is minimized by adjusting the Rx-side variable capacitor.

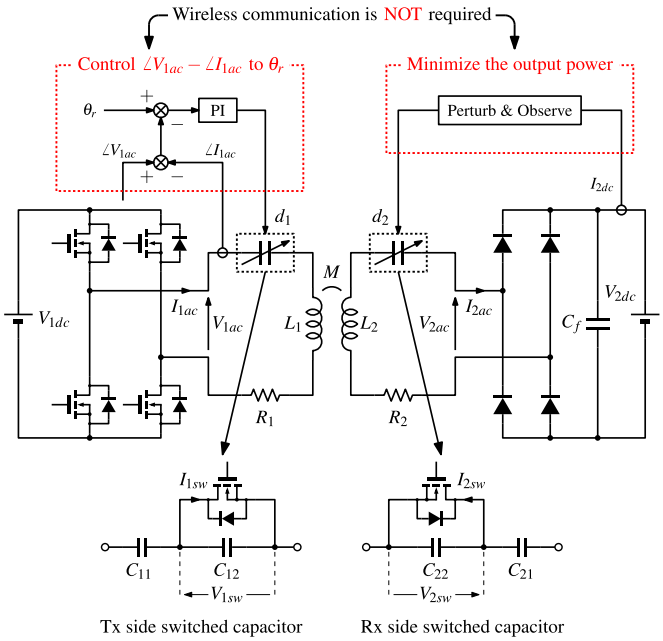

Fig. 4. Overview of the proposed control scheme to maintain the resonance condition and maximize the transmission efficiency.

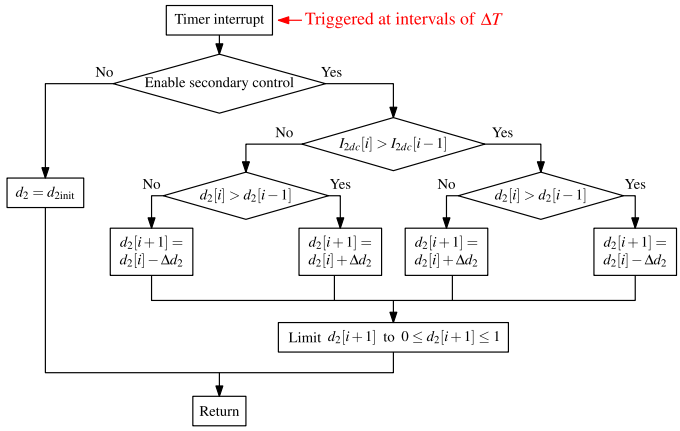

Fig. 5. Flowchart of the P&O algorithm.

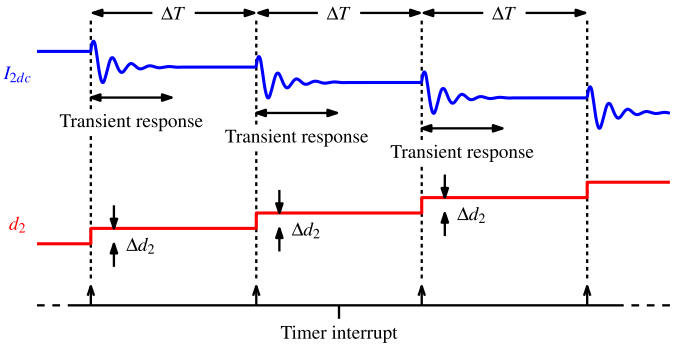

Fig. 6. Timing diagram of the P&O algorithm.

This control scheme can be explained visually based on the colormap of p_2 in Fig. 3. By controlling the phase difference between V_{1ac} and I_{1ac} to 0, x_1 and x_2 are constrained to the contour line of $\theta = 0$. Then, by tracking the minimum power point on the contour line of $\theta = 0$, x_1 and x_2 converge to the perfect resonance point, i.e., $x_1 = x_2 = 0$. As shown in Fig. 4, this control scheme can be implemented by separate closed loops on the Tx and Rx sides, thus eliminating the need for wireless communication. It should be noted that the exact target values of the variable capacitors do not need to be known in the proposed control scheme. Even if the exact values are not known, the variable capacitors automatically converge to the exact values by simultaneously performing the two functions mentioned above.

In this study, a proportional–integral (PI) controller is adopted for the Tx-side control loop, and a perturb and observe (P&O) algorithm [30] is adopted for the Rx-side control loop. The variable capacitors are realized by PWM-controlled switched capacitors.

B. Software Implementation of the Control Scheme

Since V_{2dc} is constant under the dynamics of the circuit, the output power is proportional to I_{2dc}. Therefore, as shown in Fig. 5, a P&O algorithm is adopted to search the duty cycle d_2, which yields the minimum I_{2dc}. The sequence in Fig. 5 is executed at intervals of ΔT, and d_2 is increased or decreased by a constant step size of Δd_2 in each iteration. Although not depicted in Fig. 5, a digital low-pass filter (LPF) is applied to the value of I_{2dc} to reduce the noise of the current sensor. The cutoff frequency of the LPF is set to 1 kHz.

A digital PI controller is implemented on the Tx side to regulate the phase difference between V_{1ac} and I_{1ac}. In order to avoid conflict between the PI control and the P&O algorithm, the update interval of the P&O algorithm must be designed sufficiently longer than the convergence of the PI control. This condition ensures that the phase difference between V_{1ac} and I_{1ac} is regulated to 0 and the circuit is in steady state when updating d_2 in the P&O algorithm. In other words, this condition ensures that x_1 and x_2 always stay on the contour line of $\theta = 0$ in Fig. 3 when minimizing the output power.

As shown in Fig. 6, the transient response of I_{2dc} occurs immediately after updating d_2. In order to satisfy the aforementioned condition, ΔT must be designed sufficiently longer than the settling time of I_{2dc}. In this study, the PI gains and the dc-link filter capacitor are chosen such that the settling time is shorter than 1 ms, and ΔT is set to 1 ms. Also, Δd_2 is set to 0.005.

C. PWM-Controlled Switched Capacitor

As shown in Fig. 4, the PWM-controlled switched capacitor proposed in [31] and used in [32] and [33] is adopted in this study. Compared with the PWM-controlled switched capacitor used in [14], [15], and[34], this circuit topology reduces the voltage stress across the switch, thus enabling its use in a wide range of power scales. The voltage stress is reduced since the series connection of the capacitors functions as a voltage divider.

Fig. 7 shows the current paths of four operational modes, and Fig. 8 shows the key waveforms of the switched capacitor. When

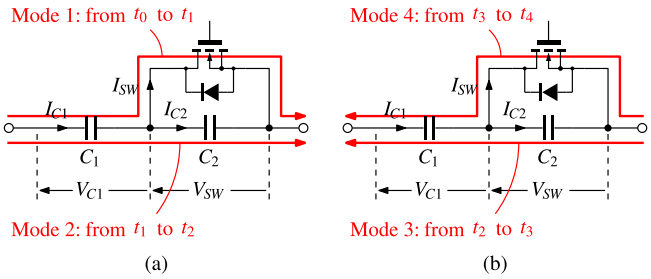

Fig. 7. Current paths of four operational modes of the PWM-controlled switched capacitor. (a) Mode 1 and Mode 2. (b) Mode 3 and Mode 4.

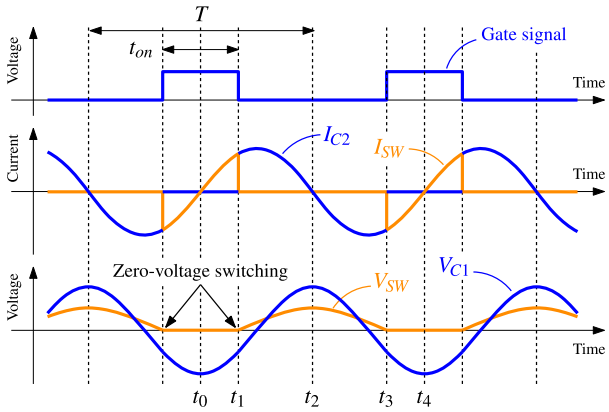

Fig. 8. Key waveforms of the PWM-controlled switched capacitor.

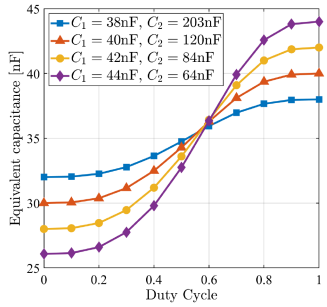

Fig. 9. Equivalent capacitance of the PWM-controlled switched capacitor as a function of the duty cycle.

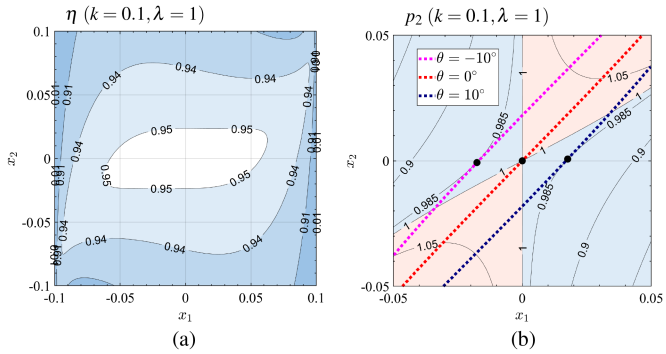

Fig. 10. Colormaps of η and p_2 as functions of x_1 and x_2 under $q_1 = q_2 = 400$, $k = 0.1$, and $\lambda = 1$. (a) Colormap of η. (b) Close-up colormap of p_2.

the switch is always turned ON, the capacitance is equal to C_1. When the switch is always turned OFF, the capacitance is equal to C_1 and C_2 in series. The equivalent capacitance can take continuous values between the two states by feeding a PWM signal synchronized with the current to the switch. It should be noted that the body diode of the MOSFET is reversely biased in Mode 2 and Mode 3. In fact, the body diode is turned OFF in all operational modes and does not affect the circuit function in terms of the fundamental harmonic. It should also be noted that the switch is turned ON and OFFwhen V_{SW} is zero, thus minimizing the switching loss.

By calculating the fundamental harmonic of $V_{C1} + V_{\mathrm{SW}}$, the equivalent capacitance of the circuit can be derived as follows:

$$C_{\mathrm{eq}} = \frac{1}{\frac{1}{C_1} + \frac{1}{C_2}\left[1 + \frac{1}{2\pi}\sin(2\pi d) - d\right]} \tag{23}$$

where the duty cycle of the gate signal is defined as $d := t_{\mathrm{on}}/T$. The detailed derivation of (23) is given in Appendix B. Fig. 9 shows the equivalent capacitance as a function of the duty cycle under four cases of C_1 and C_2. The equivalent capacitance increases nonlinearly with the duty cycle. Also, a wider range of capacitance can be achieved by reducing C_2. However, this increases the impedance of C_2, thus increasing the voltage stress across the switch. In order to prevent the electrical breakdown of the switch, this tradeoff must be considered when determining the values of C_1 and C_2.

D. Optimal Condition Considering Inverter Switching Loss

By solving KVL equations, as derived from Fig. 1, with respect to (5)–(12), the transmission efficiency can be expressed in terms of nondimensional parameters as follows:

$$\eta = \frac{P_2}{P_1} = \frac{k^2\zeta}{\frac{x_2^2}{q_1} + \left(\frac{1}{q_2} + \zeta\right)\left(\frac{\zeta}{q_1} + \frac{1}{q_1 q_2} + k^2\right)}. \tag{24}$$

Fig. 10(a) shows the colormap of η as a function of x_1 and x_2 under $q_1 = q_2 = 400$, $k = 0.1$, and $\lambda = 1$. It is well known that the efficiency does not depend on x_1 when a passive resistor is adopted as the load [16], [21]. However, Fig. 10(a) indicates that x_1 and x_2 both contribute to the decrease in the efficiency when a CV load is adopted. Therefore, it is necessary to compensate for the self-inductance variations of both the Tx and Rx coils to achieve maximum efficiency in practical applications.

It should be noted that the perfect resonance condition is not necessarily the optimal condition when considering the end-to-end system efficiency. In fact, the switching loss of the inverter is most reduced when the phase of $I_{1\mathrm{ac}}$ slightly lags the phase of $V_{1\mathrm{ac}}$ [13]. Reducing the switching loss of the inverter is essential to improve the end-to-end system efficiency, as the switching frequency is usually very high (i.e., 85 kHz) in WPT applications. Therefore, it is interesting to analyze the behavior of the proposed control scheme when the phase difference between $V_{1\mathrm{ac}}$ and $I_{1\mathrm{ac}}$ is controlled to $\theta_r \neq 0$.

By substituting (20) and $\theta = \theta_r$ into (19), the relationship between x_1 and x_2 can be derived as follows:

$$x_2 = \frac{1}{\lambda^2}x_1 - \frac{\tan\theta_r}{\lambda^2}\sqrt{\lambda^2 k^2 - x_1^2} \approx \frac{1}{\lambda^2}x_1 - \frac{k\tan\theta_r}{\lambda}. \quad (25)$$

The right-hand side of (25) is the first-order approximation of x_2 around $x_1 = 0$. By substituting (20) and (25) into (14), p_2 can be expressed in terms of x_1, k, λ, and θ_r. Then, the derivative of p_2 with respect to x_1 can be derived in the neighborhood of $x_1 = 0$ as follows:

$$\frac{dp_2}{dx_1} \approx \frac{x_1 - \lambda k\tan\theta_r}{(\lambda k + x_1\tan\theta_r)^2}. \quad (26)$$

Equations (25) and (26) indicate that the minimum point of p_2 under $\theta = \theta_r$ is given by

$$x_1 = \lambda k\tan\theta_r, \quad x_2 = 0. \quad (27)$$

In fact, x_1 and x_2 converge to (27) by minimizing the output power under $\theta = \theta_r$. It is interesting to point out that the reactance of the Rx circuit can be completely compensated even when the control target of θ is set to $\theta_r \neq 0$.

The same conclusion can also be confirmed from the close-up colormap of p_2 in Fig. 10(b). The black markers in Fig. 10(b) represent the minimum point of p_2 on the contour lines of $\theta = -10°$, $\theta = 0$, and $\theta = 10°$. Moreover, the colormaps of p_2 in Fig. 3 indicate that (27) is the global minimum point of p_2 under $\theta = \theta_r$. Therefore, it can be concluded that x_1 and x_2 converge to (27) by minimizing the output power under $\theta = \theta_r$.

The optimal θ in terms of the switching loss is usually a small positive value within the range from 0 to 10°. Fig. 10 and (27) indicate that when θ_r is within this range, x_1 and x_2 converge to the neighborhood of the perfect resonance point where the transmission efficiency is sufficiently high. Therefore, the inverter efficiency can be improved without sacrificing the ac/ac efficiency by adopting a small positive value as θ_r in the control scheme.

IV. Experimental Verification

A. Experimental Setup

A 1 kW experimental prototype of the proposed system is developed, as shown in Fig. 11. The specifications of the experimental setup are listed in Table I. The Tx and Rx coils are aligned horizontally, and the vertical gap is fixed to 100 mm. Two prototype boards of the PWM-controlled switched capacitor are fabricated, as shown in Fig. 12, and connected to the Tx and Rx circuits. SCT3030KL 1200 V/72 A SiC MOSFETs are used in the switched capacitor boards. The values of C_{11}, C_{12}, C_{21}, and C_{22} are chosen such that the equivalent capacitance of the switched capacitors varies between 31 and 40 nF. This range is adequate to achieve the perfect resonance condition when the self-inductance of the Tx and Rx coils varies between −10 and +10%. The manufacturing tolerances of electric components are typically larger than ±5%. Other factors, as mentioned in Section I, cause the self-inductance of the Tx and Rx coils to vary even more. Therefore, in this study, it is assumed that the self-inductance of the Tx and Rx coils varies between −10 and +10%. Moreover, the values of C_{11}, C_{12}, C_{21}, and C_{22} guarantee that the voltage stress across the MOSFET is sufficiently lower than 1200 V when achieving an output power of 1 kW. In the experimental results, the power and efficiency are measured using HIOKI PW6001, and the phase difference is obtained by applying fast Fourier transforms to the waveforms of the oscilloscope.

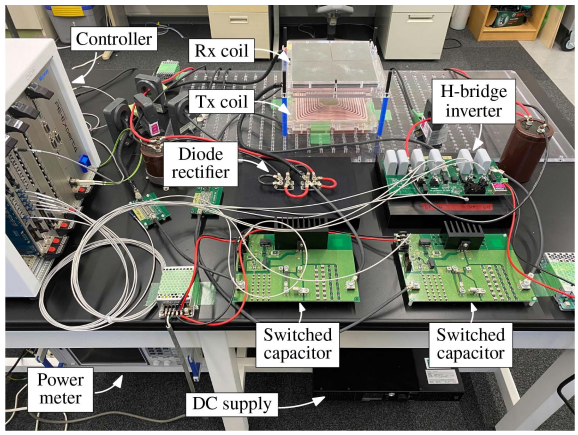

Fig. 11. Schematic diagram of the experimental setup.

TABLE I
Specifications of Experimental Setup

Description	Symbol	Value	Unit
Operating frequency	-	85.0	kHz
Tx-side dc voltage	$V_{1\mathrm{dc}}$	100	V
Rx-side dc voltage	$V_{2\mathrm{dc}}$	100	V
Self-inductance of Tx coil	L_1	99.8	μH
Self-inductance of Rx coil	L_2	101.3	μH
Mutual inductance	M	14.1	μH
ESR of Tx circuit	R_1	188	mΩ
ESR of Rx circuit	R_2	202	mΩ
DC-link filter capacitor	C_f	470	μF
Components of Tx side	C_{11}	40.1	nF
Switched capacitor	C_{12}	149.0	nF
Components of Rx side	C_{21}	39.2	nF
Switched capacitor	C_{22}	148.6	nF

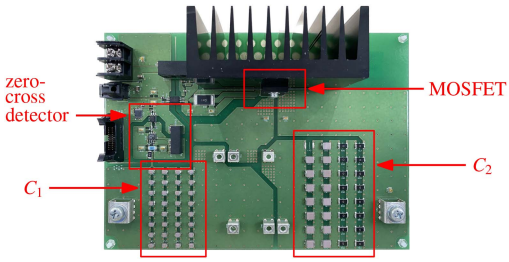

Fig. 12. Prototype board of the PWM-controlled switched capacitor.

B. Verification of the Theoretical Analysis

In order to verify the condition for perfect resonance, as derived in Section II-B, the following experiment is conducted.

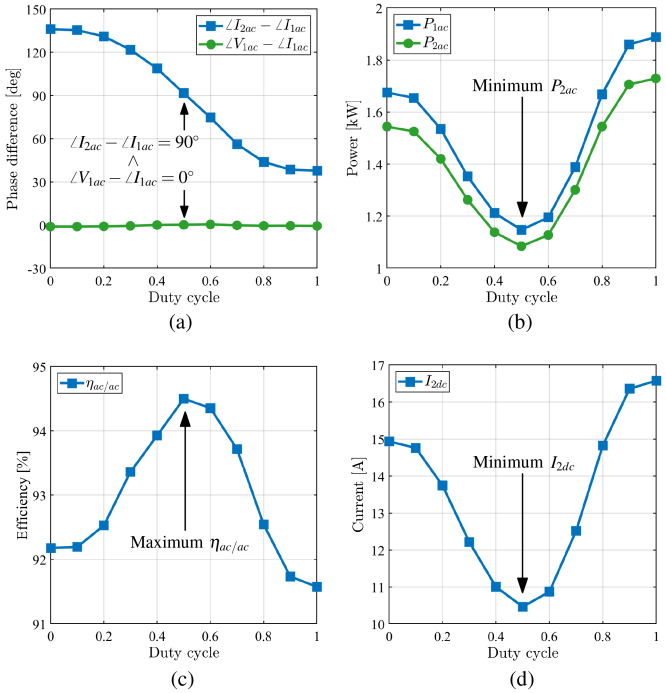

Fig. 13. Steady-state performance of the system according to d_2. (a) Phase difference among I_{1ac}, I_{2ac}, and V_{1ac}. (b) Input AC power and output AC power. (c) AC/AC efficiency. (d) Output DC current.

On the primary side, the phase difference between V_{1ac} and I_{1ac} is regulated to 0 by the PI controller. On the secondary side, the duty cycle of the switched capacitor d_2 is varied in increments of 0.1 between 0 and 1. It should be noted that the P&O algorithm is not applied in this experiment.

Fig. 13 shows the experimental results. The phase difference between I_{1ac} and I_{2ac} is approximately 90° at $d_2 = 0.5$. This means that the perfect resonance condition described in (3) is satisfied at $d_2 = 0.5$. Also, the output ac power is minimum, and the ac/ac efficiency is maximum at $d_2 = 0.5$. In fact, the perfect resonance point coincides with the minimum output power point when $\angle V_{1ac} - \angle I_{1ac}$ is regulated to 0. These results verify the condition for perfect resonance, as shown in (4). In addition, Fig. 13(d) implies that the perfect resonance point can be reached by minimizing I_{2dc} instead of P_{2ac}.

Fig. 14 shows the trajectories of d_1 and d_2 when the PI control and the P&O algorithm are both applied. The initial values of d_1 and d_2 are set to 0.3 and 0.8. The step size of d_2 in the P&O algorithm is set to 0.005, as described in Section III-B. θ_r is set to 0. In addition, Fig. 15 shows the voltage and current waveforms measured at four points $T_0, T_1, T_2,$ and T_3 in Fig. 14(b). The working principle of the proposed control scheme can be explained step-by-step as follows.

$t = T_0$: d_1 and d_2 are fixed to their initial values before the control starts. V_{1ac} and I_{1ac} are out of phase, and the phase difference between I_{1ac} and I_{2ac} is less than 90°.

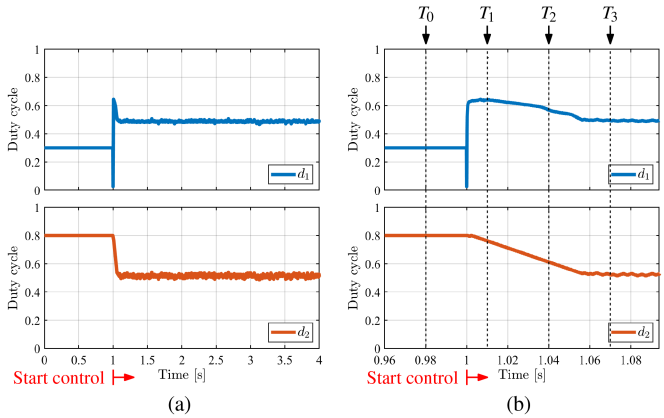

Fig. 14. Trajectories of d_1 and d_2 when applying the proposed control scheme, shown in two different time scales. (a) 0.5 s/div. (b) 0.02 s/div.

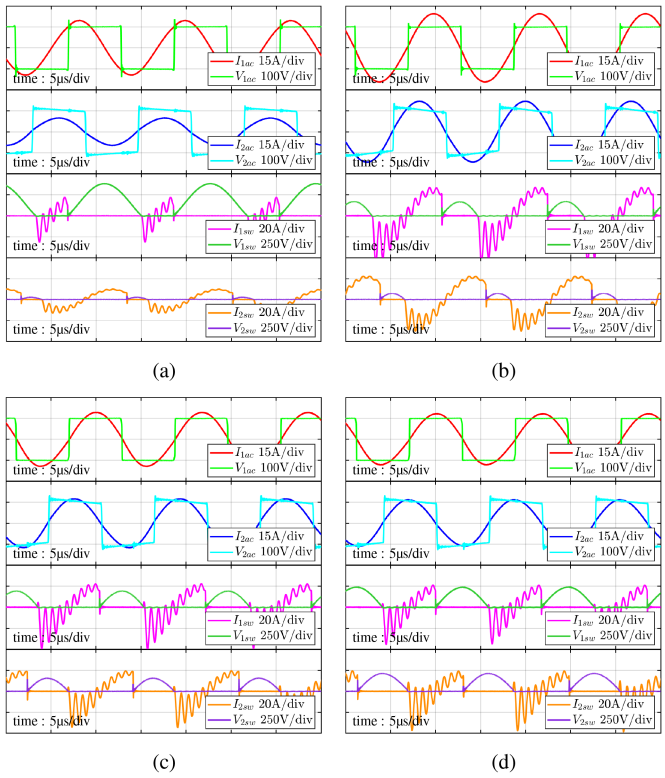

Fig. 15. Waveforms of I_{1ac}, V_{1ac}, I_{2ac}, V_{2ac}, I_{1sw}, V_{1sw}, I_{2sw}, and V_{2sw} at (a) $t = T_0$, (b) $t = T_1$, (c) $t = T_2$, and (d) $t = T_3$.

$t = T_1$: The phase difference between V_{1ac} and I_{1ac} is regulated to 0 by the PI controller. However, the phase difference between I_{1ac} and I_{2ac} is still less than 90° since the convergence of the P&O algorithm is slow compared with the PI control, as described in Section III-B.

$t = T_2$: The phase difference between V_{1ac} and I_{1ac} is maintained to 0 while the phase difference between I_{1ac} and I_{2ac} is approaching 90°. This corresponds to the output power being minimized on the contour line of $\theta = 0$ in Fig. 3.

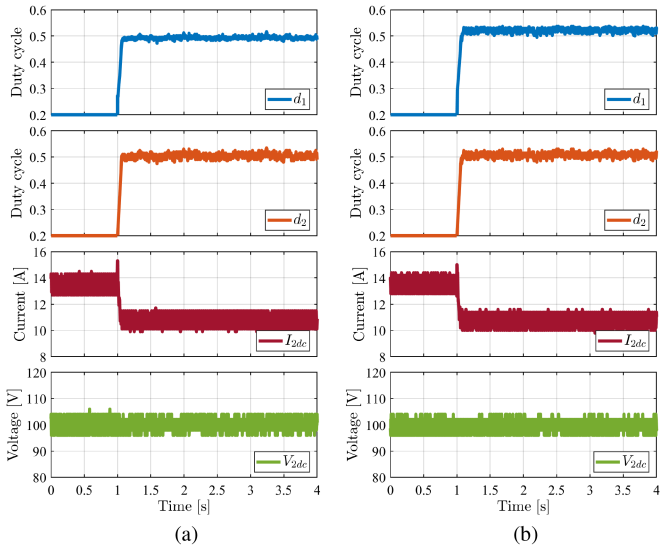

Fig. 16. Trajectories of d_1 and d_2 and waveforms of I_{2dc} and V_{2dc} when applying the proposed control scheme with (a) $\theta_r = 0$ and (b) $\theta_r = 5°$.

TABLE II
STEADY-STATE PERFORMANCE OF THE PROPOSED SYSTEM

	$\angle V_{1ac} - \angle I_{1ac}$	$\angle I_{2ac} - \angle I_{1ac}$	η_{inv}	$\eta_{ac/ac}$	$\eta_{dc/dc}$	P_{2ac}
$\theta_r = 0°$	0.5°	89.9°	98.0%	94.5%	90.4%	1.1 kW
$\theta_r = 5°$	4.8°	90.2°	98.8%	94.5%	90.8%	1.1 kW

$t = T_3$: The P&O algorithm reaches convergence and the perfect resonance condition is achieved. V_{1ac} and I_{1ac} are in phase, and the phase difference between I_{1ac} and I_{2ac} is 90°.

Fig. 16 and Table II present the comparison of applying the proposed control scheme with $\theta_r = 0$ and $\theta_r = 5°$. The initial values of d_1 and d_2 are set to 0.2. η_{inv}, $\eta_{ac/ac}$, and $\eta_{dc/dc}$ represent the inverter efficiency, the ac/ac efficiency, and the dc/dc efficiency, respectively. As shown in Fig. 16(b), when $\angle V_{1ac} - \angle I_{1ac}$ is regulated to 5°, d_1 converges to a stable value slightly higher than in Fig. 16(a). This indicates that the equivalent capacitance of the Tx-side switched capacitor is increased such that the impedance of the circuit becomes slightly inductive. As shown in Table II, $\angle I_{2ac} - \angle I_{1ac}$ converges to approximately 90° in both cases of $\theta_r = 0$ and $\theta_r = 5°$. However, the latter case achieves a higher dc/dc efficiency since the inverter efficiency is higher by 0.8% compared with the former case. These results verify the effectiveness of adopting a small positive value as θ_r in the proposed control scheme. It can also be seen from Fig. 16 that I_{2dc} settles to a stable value around 11 A, thus verifying the stability of the system output.

C. Assessment Under Diverse Patterns of Self-Inductance Variations

In order to verify the versatility of the proposed control scheme, its performance is tested against diverse patterns of self-inductance variations. Instead of directly changing the self-inductance of the coils, the values of C_{11} and C_{21} are modified to obtain the equivalent impedance, as shown in Fig. 17(a). ΔL_1 represents the self-inductance variation of the Tx coil, and C_{11}^* represents the modified value of C_{11}. In the experiment, the performance of the proposed control scheme is compared with cases in which the passive capacitors are adopted instead of switched capacitors. The passive capacitors are realized by disconnecting the MOSFETs from the switched capacitor circuits and modifying the values of C_{11} and C_{21}, as shown in Fig. 17(b). Table III lists the values of C_{11}^* and C_{21}^* corresponding to the four cases of self-inductance variations. Case A-1, A-2,... are the cases in which the switched capacitors are adopted, as shown in Fig. 17(a). Case B-1, B-2,... are the cases in which the passive capacitors are adopted, as shown in Fig. 17(b). In the experiment, θ_r is set to 5°. The initial values of d_1 and d_2 are set to 0.5.

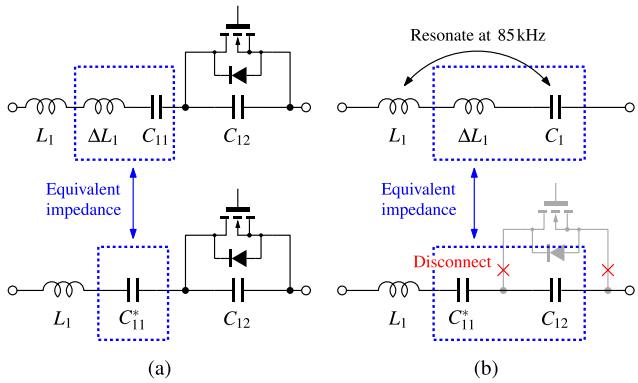

Fig. 17. Modification of C_{11} to emulate the self-inductance variation of the Tx coil connected to (a) switched capacitor and (b) passive capacitor.

TABLE III
MODIFIED VALUES OF THE SERIES-CONNECTED CAPACITORS

Case	ΔL_1	ΔL_2	C_{11}^*	C_{21}^*	Capacitor type
A-1	+10 μH	+10 μH	45.07 nF	44.22 nF	Switched
A-2	+10 μH	-10 μH	45.07 nF	35.25 nF	Switched
A-3	-10 μH	+10 μH	35.68 nF	44.22 nF	Switched
A-4	-10 μH	-10 μH	35.68 nF	35.25 nF	Switched
B-1	+10 μH	+10 μH	53.34 nF	52.17 nF	Passive
B-2	+10 μH	-10 μH	53.34 nF	40.22 nF	Passive
B-3	-10 μH	+10 μH	40.87 nF	52.17 nF	Passive
B-4	-10 μH	-10 μH	40.87 nF	40.22 nF	Passive

Fig. 18 shows the trajectories of d_1 and d_2, and Fig. 19 shows the transient response of I_{1ac}, V_{1ac}, I_{2ac}, and V_{2ac} in Cases A-1, A-2, A-3, and A-4. Figs. 20 and 21 show the voltage and current waveforms measured at steady state in the eight cases, as listed in Table III. Table IV summarizes the phase difference among V_{1ac}, I_{1ac}, and I_{2ac} in Figs. 20 and 21. As shown in Fig. 18(b), d_1 converges to ~ 0.27, and d_2 converges to ~ 0.75 in Case A-2. Compared with Fig. 16(b), d_1 is decreased to compensate for the increase in the Tx coil's self-inductance, while d_2 is increased

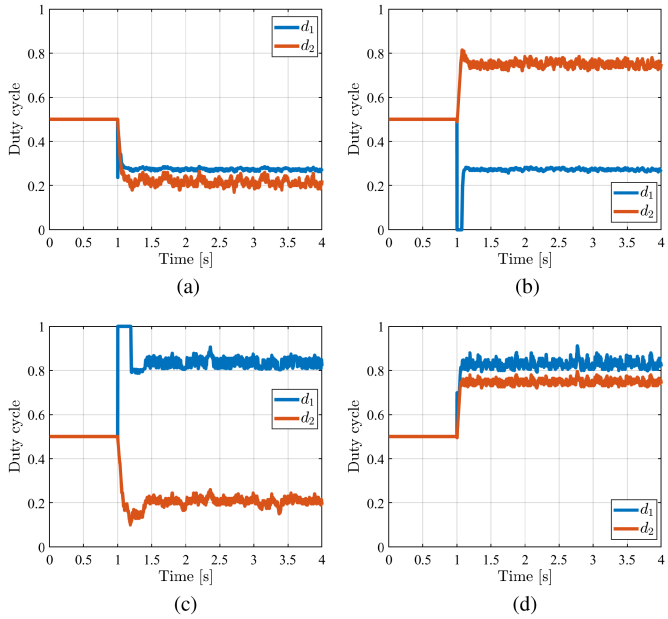

Fig. 18. Trajectories of d_1 and d_2 under four cases of self-inductance variations. (a) Case A-1. (b) Case A-2. (c) Case A-3. (d) Case A-4.

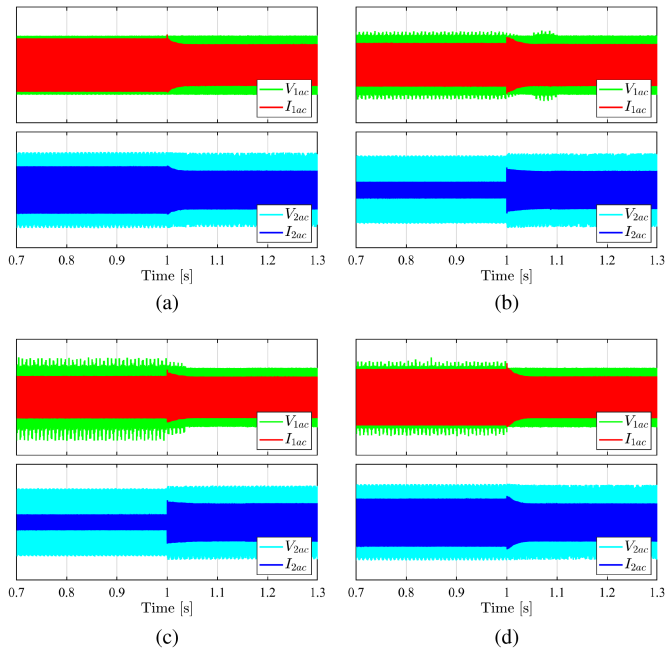

Fig. 19. Transient response of I_{1ac}, V_{1ac}, I_{2ac}, and V_{2ac}. (a) Case A-1. (b) Case A-2. (c) Case A-3. (d) Case A-4.

TABLE IV
PHASE DIFFERENCE MEASURED AT STEADY-STATE

Case	$\angle V_{1ac} - \angle I_{1ac}$	$\angle I_{2ac} - \angle I_{1ac}$	Case	$\angle V_{1ac} - \angle I_{1ac}$	$\angle I_{2ac} - \angle I_{1ac}$
A-1	5.09°	90.84°	B-1	13.83°	45.16°
A-2	4.95°	90.46°	B-2	67.93°	104.91°
A-3	5.08°	91.56°	B-3	−60.68°	71.90°
A-4	4.76°	89.89°	B-4	−11.25°	125.35°

to compensate for the decrease in the Rx coil's self-inductance. Similarly, the behaviors of d_1 and d_2 in Fig. 18(a), (c), and (d) all reflect the values of ΔL_1 and ΔL_2, as listed in Table III. The waveforms in Fig. 19 indicate that I_{1ac}, V_{1ac}, I_{2ac}, and V_{2ac} are stabilized in less than 100 ms after the control starts. As shown in Fig. 20 and Table IV, $\angle V_{1ac} - \angle I_{1ac}$ converges to approximately 5°, and $\angle I_{2ac} - \angle I_{1ac}$ converges to approximately 90° in Cases A-1, A-2, A-3, and A-4. On the other hand, as shown in Fig. 21 and Table IV, the phase difference among $\angle V_{1ac}$, $\angle I_{1ac}$, and $\angle I_{2ac}$ is far from optimal in Cases B-1, B-2, B-3, and B-4. These results show that the proposed control scheme can flexibly adapt to diverse patterns of self-inductance variations and maintain the resonance condition.

As shown in Fig. 20, small vibrations appear in the waveforms of I_{1sw} and I_{2sw} immediately after the MOSFET turns ON. These vibrations are caused by the parasitic inductance in the switched capacitor board. However, the overall system performance is unaffected since the vibrations occur locally within the switched capacitor circuit. Moreover, the peak values of V_{1sw} and V_{2sw} are sufficiently lower than the MOSFET voltage rating. These waveforms verify the functionality of the PWM-controlled switched capacitor.

Fig. 22(a) and (b) shows the ac/ac efficiency and dc/dc efficiency in the eight cases, as listed in Table III, all of which are measured at steady state. When passive capacitors are adopted (i.e., Cases B-1, B-2,...), the ac/ac efficiency and dc/dc efficiency vary significantly depending on the self-inductance variations. On the other hand, when the proposed control scheme is applied (*i.e.* Case A-1, A-2,...), the system maintains a stable ac/ac efficiency and dc/dc efficiency regardless of the self-inductance variations. The comparison of Cases A-2 and B-2 indicates that the ac/ac efficiency and dc/dc efficiency are increased by 3.59% and 4.98%, respectively, by applying the proposed control scheme under $\Delta L_1 = +10\,\mu$H and $\Delta L_2 = -10\,\mu$H. The ac/ac efficiency is increased since the system operates near the perfect resonance point by applying the proposed control scheme. The additional increase in the dc/dc efficiency results from the reduction in the switching loss of the inverter. The same argument can be applied to the other three cases of self-inductance variations. These results verify that the proposed system can maintain a high end-to-end system efficiency by flexibly adapting to the self-inductance variations of the Tx and Rx coils.

Fig. 23 shows the loss distribution of the system measured at steady state in Cases A-1, A-2, A-3, and A-4. Since it is difficult to directly measure the loss of the switched capacitors, the loss of the switched capacitors is estimated by subtracting the ac loss of the circuit with optimal passive capacitors from the ac loss of the circuit with switched capacitors. The loss of the inverter, the WPT coils, and the rectifier are roughly the same among the four cases. On the other hand, there is a noticeable difference in the loss of the switched capacitors. The main reason for this is the difference in the conduction time of the MOSFETs. As shown in Fig. 18, the final values of d_1 and d_2 in Case A-4 are the highest among the four cases, resulting in the longest conduction time of the MOSFETs. However, in either case, the loss of the switched capacitors is sufficiently small compared with the loss of the

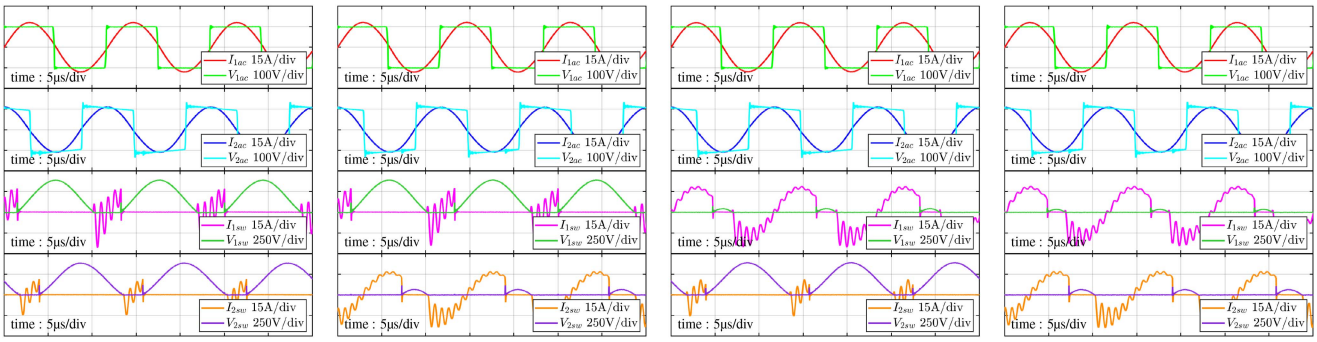

Fig. 20. Waveforms of I_{1ac}, V_{1ac}, I_{2ac}, V_{2ac}, I_{1sw}, V_{1sw}, I_{2sw}, and V_{2sw} after convergence in (a) Case A-1, (b) Case A-2, (c) Case A-3, and (d) Case A-4.

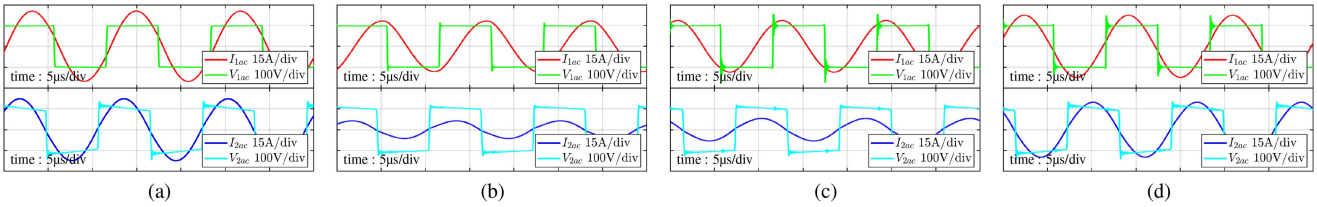

Fig. 21. Waveforms of I_{1ac}, V_{1ac}, I_{2ac}, and V_{2ac} in (a) Case B-1, (b) Case B-2, (c) Case B-3, and (d) Case B-4.

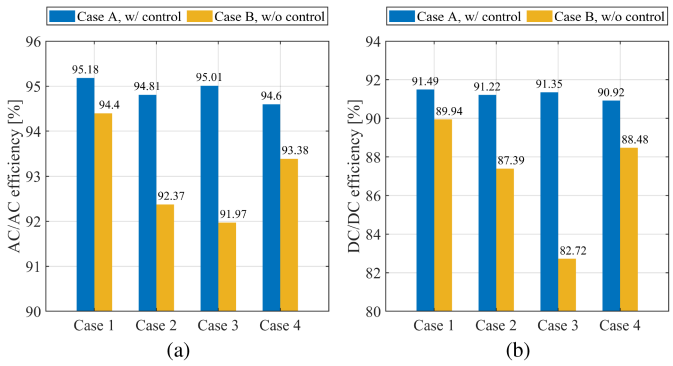

Fig. 22. (a) AC/AC efficiency and (b) DC/DC efficiency measured at steady state under four cases of self-inductance variations.

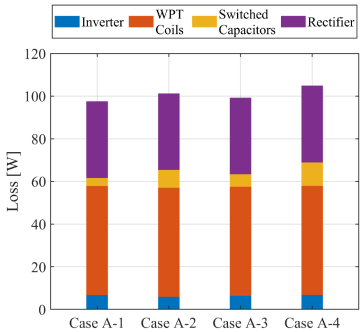

Fig. 23. Loss distribution measured at steady state when the proposed control scheme is applied against four cases of self-inductance variations.

WPT coils, indicating that the switched capacitors have only minor negative effects on the system efficiency.

V. Conclusion

In this article, a control scheme for PWM-controlled switched capacitors was proposed to compensate for the self-inductance variations of the Tx and Rx coils without wireless communication. The novelty of this article is a unique condition for perfect resonance, which was derived by focusing on the output power of the WPT circuit. Based on this condition, the switched capacitors can be controlled simultaneously by separate closed loops on the Tx and Rx sides, thus eliminating the need for wireless communication. The condition for perfect resonance was experimentally verified using a 1-kW prototype of the proposed system. The experimental results also revealed that the switched capacitors can flexibly adapt to diverse patterns of self-inductance variations and maintain the resonance condition. The ac/ac efficiency and dc/dc efficiency were both improved compared with the cases in which passive capacitors were adopted.

The condition for perfect resonance and the basic concept of the control scheme can generally be applied to any S–S compensated WPT system interfacing CV dc buses. It should be noted that the optimal charging process of batteries, i.e., constant current (CC) and CV charging [22], [34], was not considered in this article. The integration of the proposed control scheme with CC and CV charging is an important topic for future research. Other future works include the investigation of variable capacitor circuits applicable to higher power levels and the optimization of control parameters to improve the response speed.

APPENDIX A

By applying KVL to the circuit in Fig. 1, the following equations can be obtained:

$$\dot{V}_{1\mathrm{ac}} = \left(j\omega L_1 + \frac{1}{j\omega C_1} + R_1\right)\dot{I}_{1\mathrm{ac}} - j\omega M\dot{I}_{2\mathrm{ac}} \tag{A1}$$

$$\dot{V}_{2\mathrm{ac}} = j\omega M\dot{I}_{1\mathrm{ac}} - \left(j\omega L_2 + \frac{1}{j\omega C_2} + R_2\right)\dot{I}_{2\mathrm{ac}}. \tag{A2}$$

The equivalent load resistance of the circuit is defined as follows:

$$R_L := \frac{\dot{V}_{2\mathrm{ac}}}{\dot{I}_{2\mathrm{ac}}}. \tag{A3}$$

It should be noted that when $V_{2\mathrm{dc}}$ is constant, R_L is not constant and can vary depending on other circuit parameters, such as X_1, X_2, and M. This causes a significant difference in the circuit characteristics when compared with modeling the load as a passive resistor. By substituting (A3) into (A1) and (A2), R_L can be expressed in terms of the constants defined in Figs. 1 and 2, and (7) as follows:

$$R_L = \frac{B + \sqrt{B^2 + AC}}{A} \tag{A4}$$

where

$$A := \frac{V_{1\mathrm{dc}}^2}{V_{2\mathrm{dc}}^2}(\omega M)^2 - R_1^2 - X_1^2 \tag{A5}$$

$$B := R_1\left[R_1R_2 + (\omega M)^2\right] + R_2X_1X_2 \tag{A6}$$

$$C := \left[R_1R_2 + (\omega M)^2 - X_1X_2\right]^2 + (R_1X_2 + R_2X_1)^2. \tag{A7}$$

The input power and the output power can be expressed using R_L as follows:

$$P_1 = R_1|\dot{I}_{1\mathrm{ac}}|^2 + R_2|\dot{I}_{2\mathrm{ac}}|^2 + \frac{|\dot{V}_{2\mathrm{ac}}|^2}{R_L} \tag{A8}$$

$$P_2 = \frac{|\dot{V}_{2\mathrm{ac}}|^2}{R_L}. \tag{A9}$$

From (A1)–(A3), P_1 can be rewritten as follows:

$$P_1 = \left[\frac{X_2^2 + (R_2 + R_L)^2}{R_L^2(\omega M)^2}R_1 + \frac{R_2}{R_L^2} + \frac{1}{R_L}\right]|\dot{V}_{2\mathrm{ac}}|^2. \tag{A10}$$

By substituting (A4)–(A7) into (A9) and (A10), P_1 and P_2 can be expressed without using R_L. Finally, the per-unit expressions of P_1 and P_2 can be derived using the definitions in (8)–(12) as in (13) and (14).

The impedance at the input of the circuit in Fig. 1 can be expressed using R_L as follows:

$$Z_{\mathrm{in}} = \frac{R_L(\omega M)^2}{R_L^2 + X_2^2} + j\left[X_1 - \frac{X_2(\omega M)^2}{R_L^2 + X_2^2}\right]. \tag{A11}$$

Therefore, the phase difference between $\dot{V}_{1\mathrm{ac}}$ and $\dot{I}_{1\mathrm{ac}}$ can be expressed using the definitions in (8)–(12) as follows:

$$\theta = \arctan\left(\frac{\mathrm{Im}\left[Z_{\mathrm{in}}\right]}{\mathrm{Re}\left[Z_{\mathrm{in}}\right]}\right) = \arctan\left(\frac{x_1\left(\zeta^2 + x_2^2\right) - x_2k^2}{\zeta k^2}\right). \tag{A12}$$

APPENDIX B

Due to the bandpass characteristic of the resonant network, I_{C1} in Fig. 7 can be approximated as a sine wave as follows:

$$I_{C1} = A\sin\left(\frac{2\pi}{T}t\right) \tag{B1}$$

where A is the amplitude and T is the period of I_{C1}. Therefore, V_{C1} can be expressed as follows:

$$V_{C1} = -\frac{AT}{2\pi C_1}\cos\left(\frac{2\pi}{T}t\right) \tag{B2}$$

and V_{SW} can be expressed as follows:

$$V_{\mathrm{SW}} = \begin{cases} 0 & : \text{in Mode 1 and Mode 4} \\ \dfrac{1}{C_2}\int_{t_1}^{t} I_{C1}dt & : \text{in Mode 2 and Mode 3.} \end{cases} \tag{B3}$$

From (B1)–(B3), the fundamental harmonic of $V_{C1} + V_{\mathrm{SW}}$ can be derived by Fourier series expansion

$$\begin{aligned} V_{fh} &= \frac{2}{T}\int_{t_0}^{t_4}(V_{C1} + V_{\mathrm{SW}})\cos\left(\frac{2\pi}{T}t\right)dt \\ &= -\frac{AT}{2\pi}\left\{\frac{1}{C_1} + \frac{1}{C_2}\left[1 + \frac{1}{2\pi}\sin(2\pi d) - d\right]\right\} \end{aligned} \tag{B4}$$

where d is the duty cycle of the PWM signal. Therefore, the equivalent capacitance of the switched capacitor circuit can be expressed in terms of d as follows:

$$C_{\mathrm{eq}} = -\frac{A}{V_{fh}} \times \frac{T}{2\pi} = \frac{1}{\frac{1}{C_1} + \frac{1}{C_2}\left[1 + \frac{1}{2\pi}\sin(2\pi d) - d\right]}. \tag{B5}$$

REFERENCES

[1] Y. Jang and M. M. Jovanovic, "A contactless electrical energy transmission system for portable-telephone battery chargers," *IEEE Trans. Ind. Electron.*, vol. 50, no. 3, pp. 520–527, Jun. 2003.

[2] M. Sato, G. Yamamoto, D. Gunji, T. Imura, and H. Fujimoto, "Development of wireless in-wheel motor using magnetic resonance coupling," *IEEE Trans. Power Electron.*, vol. 31, no. 7, pp. 5270–5278, Jul. 2016.

[3] A. Kurs, A. Karalis, R. Moffatt, J. D. Joannopoulos, P. Fisher, and M. Soljačić, "Wireless power transfer via strongly coupled magnetic resonances," *Science*, vol. 317, no. 5834, pp. 83–86, 2007.

[4] T. Imura and Y. Hori, "Maximizing air gap and efficiency of magnetic resonant coupling for wireless power transfer using equivalent circuit and Neumann formula," *IEEE Trans. Ind. Electron.*, vol. 58, no. 10, pp. 4746–4752, Oct. 2011.

[5] W. Zhang and C. C. Mi, "Compensation topologies of high-power wireless power transfer systems," *IEEE Trans. Veh. Technol.*, vol. 65, no. 6, pp. 4768–4778, Jun. 2016.

[6] "Wireless power transfer for light-duty plug-in/electric vehicles and alignment methodology," SAE International, Warrendale, PA, USA, 2022, doi: 10.4271/J2954_202208.

[7] S. Y. Jeong, J. H. Park, G. P. Hong, and C. T. Rim, "Autotuning control system by variation of self-inductance for dynamic wireless EV charging with small air gap," *IEEE Trans. Power Electron.*, vol. 34, no. 6, pp. 5165–5174, Jun. 2019.

[8] S. Y. Jeong, V. X. Thai, J. H. Park, and C. T. Rim, "Self-inductance-based metal object detection with mistuned resonant circuits and nullifying induced voltage for wireless EV chargers," *IEEE Trans. Power Electron.*, vol. 34, no. 1, pp. 748–758, Jan. 2019.

[9] J. Lu, G. Zhu, and C. C. Mi, "Foreign object detection in wireless power transfer systems," *IEEE Trans. Ind. Appl.*, vol. 58, no. 1, pp. 1340–1354, Jan./Feb. 2022.

[10] G. A. Covic, J. T. Boys, A. M. W. Tam, and J. C.-H. Peng, "Self tuning pick-ups for inductive power transfer," in *Proc. IEEE Power Electron. Specialists Conf.*, 2008, pp. 3489–3494.
[11] T. C. Beh, M. Kato, T. Imura, S. Oh, and Y. Hori, "Automated impedance matching system for robust wireless power transfer via magnetic resonance coupling," *IEEE Trans. Ind. Electron.*, vol. 60, no. 9, pp. 3689–3698, Sep. 2013.
[12] Y. Lim, H. Tang, S. Lim, and J. Park, "An adaptive impedance-matching network based on a novel capacitor matrix for wireless power transfer," *IEEE Trans. Power Electron.*, vol. 29, no. 8, pp. 4403–4413, Aug. 2014.
[13] J. Osawa, T. Isobe, and H. Tadano, "Efficiency improvement of high frequency inverter for wireless power transfer system using a series reactive power compensator," in *Proc. IEEE 12th Int. Conf. Power Electron. Drive Syst.*, 2017, pp. 992–998.
[14] D.-H. Kim and D. Ahn, "Self-tuning LCC inverter using PWM-controlled switched capacitor for inductive wireless power transfer," *IEEE Trans. Ind. Electron.*, vol. 66, no. 5, pp. 3983–3992, May 2019.
[15] H. Zhang, Y. Chen, C.-H. Jo, S.-J. Park, and D.-H. Kim, "DC-link and switched capacitor control for varying coupling conditions in inductive power transfer system for unmanned aerial vehicles," *IEEE Trans. Power Electron.*, vol. 36, no. 5, pp. 5108–5120, May 2021.
[16] J. Zhang, J. Zhao, Y. Zhang, and F. Deng, "A wireless power transfer system with dual switch-controlled capacitors for efficiency optimization," *IEEE Trans. Power Electron.*, vol. 35, no. 6, pp. 6091–6101, Jun. 2020.
[17] W. Li, G. Wei, C. Cui, X. Zhang, and Q. Zhang, "A double-side self-tuning LCC/S system using a variable switched capacitor based on parameter recognition," *IEEE Trans. Ind. Electron.*, vol. 68, no. 4, pp. 3069–3078, Apr. 2021.
[18] W. Li, Q. Zhang, C. Cui, and G. Wei, "A self-tuning S/S compensation WPT system without parameter recognition," *IEEE Trans. Ind. Electron.*, vol. 69, no. 7, pp. 6741–6750, Jul. 2022.
[19] A. Berger, M. Agostinelli, S. Vesti, J. A. Oliver, J. A. Cobos, and M. Huemer, "A wireless charging system applying phase-shift and amplitude control to maximize efficiency and extractable power," *IEEE Trans. Power Electron.*, vol. 30, no. 11, pp. 6338–6348, Nov. 2015.
[20] K. Colak, E. Asa, M. Bojarski, D. Czarkowski, and O. C. Onar, "A novel phase-shift control of semibridgeless active rectifier for wireless power transfer," *IEEE Trans. Power Electron.*, vol. 30, no. 11, pp. 6288–6297, Nov. 2015.
[21] R. Mai, Y. Liu, Y. Li, P. Yue, G. Cao, and Z. He, "An active-rectifier-based maximum efficiency tracking method using an additional measurement coil for wireless power transfer," *IEEE Trans. Power Electron.*, vol. 33, no. 1, pp. 716–728, Jan. 2018.
[22] S. Ann and B. K. Lee, "Analysis of impedance tuning control and synchronous switching technique for a semibridgeless active rectifier in inductive power transfer systems for electric vehicles," *IEEE Trans. Power Electron.*, vol. 36, no. 8, pp. 8786–8798, Aug. 2021.
[23] M. Ishihara, K. Fujiki, K. Umetani, and E. Hiraki, "Autonomous system concept of multiple-receiver inductive coupling wireless power transfer for output power stabilization against cross-interference among receivers and resonance frequency tolerance," *IEEE Trans. Ind. Appl.*, vol. 57, no. 4, pp. 3898–3910, Jul./Aug. 2021.
[24] X. Xie, C. Xie, Y. Li, J. Wang, Y. Du, and L. Li, "Adaptive decoupling between receivers of multireceiver wireless power transfer system using variable switched capacitor," *IEEE Trans. Transp. Electrific.*, vol. 7, no. 4, pp. 2143–2155, Dec. 2021.
[25] R. Matsumoto and H. Fujimoto, "Adaptive compensation scheme for wireless power transfer systems with coil inductance variation using PWM-controlled switched capacitor," in *Proc. Wireless Power Week*, 2022, pp. 244–248.
[26] Z. Ma, M. Xiao, Y. Xiao, Z. Pang, H. V. Poor, and B. Vucetic, "High-reliability and low-latency wireless communication for Internet of Things: Challenges, fundamentals, and enabling technologies," *IEEE Internet Things J.*, vol. 6, no. 5, pp. 7946–7970, Oct. 2019.
[27] D. Patil, M. K. McDonough, J. M. Miller, B. Fahimi, and P. T. Balsara, "Wireless power transfer for vehicular applications: Overview and challenges," *IEEE Trans. Transp. Electrific.*, vol. 4, no. 1, pp. 3–37, Mar. 2018.
[28] G. Guidi and J. A. Suul, "Minimizing converter requirements of inductive power transfer systems with constant voltage load and variable coupling conditions," *IEEE Trans. Ind. Electron.*, vol. 63, no. 11, pp. 6835–6844, Nov. 2016.
[29] J. Zhou, G. Guidi, K. Ljøkelsøy, and J. A. Suul, "Evaluation and suppression of oscillations in inductive power transfer systems with constant voltage load and pulse skipping modulation," *IEEE Trans. Power Electron.*, vol. 38, no. 8, pp. 10412–10425, Aug. 2023.
[30] N. Femia, G. Petrone, G. Spagnuolo, and M. Vitelli, "Optimization of perturb and observe maximum power point tracking method," *IEEE Trans. Power Electron.*, vol. 20, no. 4, pp. 963–973, Jul. 2005.
[31] W.-J. Gu and K. Harada, "A new method to regulate resonant converters," *IEEE Trans. Power Electron.*, vol. 3, no. 4, pp. 430–439, Oct. 1988.
[32] R. Matsumoto and H. Fujimoto, "Wireless EV charging system using PWM-controlled variable capacitor for maximum power transfer under severe coil misalignment," in *Proc. Int. Power Electron. Conf.*, 2022, pp. 1476–1480.
[33] F. Grazian, T. B. Soeiro, and P. Bauer, "Inductive power transfer based on variable compensation capacitance to achieve an EV charging profile with constant optimum load," *IEEE J. Emerg. Sel. Topics Power Electron.*, vol. 11, no. 1, pp. 1230–1244, Feb. 2023.
[34] U. D. Kavimandan, S. M. Mahajan, and C. W. van Neste, "Analysis and demonstration of a dynamic ZVS angle control using a tuning capacitor in a wireless power transfer system," *IEEE J. Emerg. Sel. Topics Power Electron.*, vol. 9, no. 2, pp. 1876–1890, Apr. 2021.

Ryo Matsumoto (Graduate Student Member, IEEE) received the B.E. degree in electrical and electronic engineering from The University of Tokyo, Tokyo, Japan, in 2020, and the M.S. degree in advanced energy engineering in 2022 from the Department of Advanced Energy, Graduate School of Frontier Sciences, The University of Tokyo, Kashiwa, Japan, where he is currently working toward the Ph.D. degree.

His current research interests include wireless power transfer and power electronics.

Mr. Matsumoto was the recipient of the Best Paper Awards First Prize at the 2022 IEEE Wireless Power Week.

Toshiyuki Fujita (Member, IEEE) received the B.S. degree in electrical engineering, the M.S. degree in physical electronics, and the Ph.D degree in electrical and electronic engineering from the Tokyo Institute of Technology, Tokyo, Japan, in 2008, 2010, and 2017, respectively.

Since 2014, he has been with Technova, Inc., Tokyo, Japan. He was with Panasonic Corporation, Osaka, Japan, from 2010 to 2014. In 2019, he joined the University of Tokyo, Chiba, Japan, as a Project Assistant Professor. His research interests include WPT systems for electric vehicles, ac/dc converters, and its control methods.

Dr. Fujita is a member of IEE Japan, the Society of Automotive Engineers of Japan, and the Japan Society of Applied Physics.

Hiroshi Fujimoto (Senior Member, IEEE) received the Ph.D. degree in electrical engineering from the Department of Electrical Engineering, The University of Tokyo, Kashiwa, Japan, in 2001.

In 2001, he joined the Department of Electrical Engineering, Nagaoka University of Technology, Niigata, Japan, as a Research Associate. From 2002 to 2003, he was a Visiting Scholar with the School of Mechanical Engineering, Purdue University, West Lafayette, IN, USA. In 2004, he joined the Department of Electrical and Computer Engineering, Yokohama National University, Yokohama, Japan, as a Lecturer, and became an Associate Professor in 2005. He was an Associate Professor with The University of Tokyo from 2010 to 2020 and has been a Professor since 2021. His interests include control engineering, motion control, nanoscale servo systems, electric vehicle control, motor drive, visual servoing, and wireless motors.

Dr. Fujimoto was a recipient of the Best Paper Award from the IEEE TRANSACTIONS ON INDUSTRIAL ELECTRONICS in 2001 and 2013, Isao Takahashi Power Electronics Award in 2010, Best Author Prize of SICE in 2010, the Nagamori Grand Award in 2016, and First Prize Paper Award for the IEEE TRANSACTIONS ON POWER ELECTRONICS in 2016. He is a Senior Member of the IEE of Japan. He is also a member of the Society of Instrument and Control Engineers, Robotics Society of Japan, and Society of Automotive Engineers of Japan. He has been a Senior Editor for the IEEE/ASME TRANSACTIONS ON MECHATRONICS since 2022 and an Associate Editor for the IEEE Industrial Electronics Magazine since 2006. He has been a Chairperson of the JSAE Technology Board since 2022 and was a past Chairperson of the IEEE/IES Technical Committee on Motion Control from 2012 to 2013.